Communication

Microcompression Behaviors of Single Crystals Simulated by Crystal Plasticity Finite Element Method

JAE-HO JUNG, YOUNG-SANG NA,
KYUNG-MOX CHO, DENNIS M. DIMIDUK,
and YOON SUK CHOI

The microcompression behavior of single-slip oriented, single-crystal micro-pillars was simulated using a crystal plasticity finite element method, by varying a primary slip-plane inclination angle from 36.3 to 48.7 deg while keeping the same primary slip system. Simulated global deformation of the micro-pillars was separated into two types, depending upon the primary slip-plane inclination angle: the one consistent with the primary slip direction and the other diagonally opposite to the primary slip direction.

The early investigation of the materials "size effect" was mainly performed by mechanically testing (particularly, micro-compression testing) single-crystal micro-pillars, which were mechanically machined or electrochemically fabricated from bulk materials.[1–7] Since the microcompression test of single-crystal micro-pillars is different from the standardized compression test, which uses 'bulk' specimens, the crystal plasticity finite element method (CP-FEM) was frequently used for the parametric study of compressive deformation behavior of single-crystal micro-pillars.[4,8–13] Here, the bottom end of the single-crystal micro-pillar is intrinsically constrained in its lateral deformation. Thus, CP-FEM simulations aimed mostly at understanding the effect of bottom-end constraints, applied boundary conditions, and the sensitivity of the choice of constitutive models. In particular, these simulations were mainly for the compressive deformation of single-slip-oriented micro-pillars. Even though the slip system kinematics and kinetics are incorporated in CP-FEM, FEM is still limited to a continuum representation of deformation, which lacks representing slip at the crystal defect scale and the discrete nature of slip intermittency in single crystals.

In the present study, an effort was made to clarify how the CP-FEM predicts single-slip-dominated microcompression behaviors of single crystals under the different single-slip configurations (by varying the degree of primary slip-plane inclination). An elasto-viscoplasticity constitutive model was developed, based upon the combination of conventional slip system kinematics and kinetics equations, and used for the current simulations. Simulation results were analyzed as a function of primary slip-plane inclination angles and discussed.

An elasto-viscoplasticity constitutive model used for the current CP-FEM simulation utilized a Power-law shear rate description

$$\dot{\gamma}^{\alpha} = \dot{\gamma}_o \left| \frac{\tau^{\alpha}}{\hat{g}^{\alpha}} \right|^{1/m} \text{sign}(\tau^{\alpha}). \quad [1]$$

Here, $\dot{\gamma}^{\alpha}$ and $\hat{g}^{\alpha}$ are the shear rate and slip resistance for the slip system α, respectively. Also, $\dot{\gamma}_o$, τ^{α} and m are the reference shear rate, the resolved shear stress on the slip system α and the strain-rate sensitivity parameter, respectively. In Eq. [1], the slip resistance $\hat{g}^{\alpha}$ was described by a Baily–Hirsch type flow stress description[15,16] modified to account for anisotropic slip system interactions:

$$\hat{g}^{\alpha} = \hat{g}_o + \eta\mu b \sqrt{\sum_{\beta=1}^{12} A^{\alpha\beta} \rho^{\beta}}. \quad [2]$$

Here, $\hat{g}_o$, η, μ, and b are the critical resolved shear stress, a geometry constant, the shear modulus, and the magnitude of Burgers vector, respectively. Also, $A^{\alpha\beta}$ is the slip strength interaction coefficient, and ρ^{β} is the dislocation density on the slip system β. The slip strength interaction coefficient $A^{\alpha\beta}$ quantifies the influence of the activity of the slip system β on the slip resistance of the slip system α.[14,17,18] For octahedral slip systems, six characteristic slip strength interaction types have been reported:[19,20] self-hardening (A_{SH}), coplanar hardening (A_{CO}), cross-slip hardening (A_{CS}), Hirth lock (A_{HL}), Glissile lock (A_{GL}) and Lomer–Cottrell lock (A_{LC}). For the description of the dislocation density evolution, the Kocks–Mecking–Estrin equation[21,22] was used:

$$\dot{\rho}^{\alpha} = \left\{ k_1 \sqrt{\rho^{\alpha}} - k_2 \rho^{\alpha} \right\} |\dot{\gamma}^{\alpha}|, \quad [3]$$

where k_1 is the parameter related with the athermal storage of dislocation density (forest), which accounts for the stage II hardening, and k_2 is the parameter

JAE-HO JUNG, Graduate Student, KYUNG-MOX CHO, Professor, and YOON SUK CHOI, Associate Professor, are with the School of Materials Science & Engineering, Pusan National University, Busan 609-735, Korea. Contact email: choiys@pusan.ac.kr YOUNG-SANG NA, Senior Researcher, is with the Korea Institute of Materials Science, Changwon, Gyeongnam 642-831, Korea. DENNIS M. DIMIDUK, Consultant, is with BlueQuartz Software, LLC, 400 South Pioneer Blvd., Springboro, OH 45066.

associated with the reduction of dislocation density due to the dynamic recovery (the stage III hardening). Constitutive Eqs. [1] to [3] were implemented in the commercial FEM tool ABAQUS® through the User MATerial subroutine (UMAT). Here, the tangent modulus method[16,23,24] was used for the numerical integration. Twelve octahedral slip systems used for the constitutive model are listed in Table I.

The present numerical study is intended to understand how CP-FEM predicts single-slip-dominated microcompression behaviors of single-crystal micro-pillars under different single-slip configurations. For this purpose, a slip-plane inclination angle (θ) was introduced such that θ measures an angle between the primary slip plane and the top surface of the single-crystal micro-pillar, which contacts the platen upon microcompression. For the representation of different single-slip configurations, five crystal orientations were carefully chosen such that θ varies from 36.3 to 48.7 deg and each orientation has a primary slip system ($(111)[\bar{1}01]$) having a Schmid factor difference (ΔSF) between the primary and secondary slip systems larger than 0.043 (to ensure single-slip-dominated compressive deformation). Bunge–Euler angles for these five orientations are listed in Table II. For these five orientations, microcompression tests were simulated using CP-FEM with the elasto-viscoplastic constitutive model described above. Figure 1 shows the simulation geometry of the micro-pillar and the platen. Here, note that the primary slip direction is $[\bar{1}01]$ for all θs, making the X-axis in the sample coordinate being $[1\bar{2}1]$. The sample material parameters were chosen to be those for a Ni-base single-crystal superalloy. The height-to-diameter ratio of the micro-pillar was set to be 2.3. The microcompression was simulated by moving the platen (which is considered as a rigid body) downward at a constant speed. Here, the friction-free condition was applied for the contact between the top surface of the micro-pillar and the platen. The target axial strain was 0.1, and the strain rate was set to be 10^{-3}/s. Table III summarizes values of major input parameters. Here, some input parameter values were chosen such that no significant strain hardening was intentionally introduced from constitutive equations (Eqs. [2] and [3]). In this sense, any observable hardening and/or softening from CP-FEM simulations would be mainly due to the deformation geometry effect of single-slip-oriented micro-pillars combined with applied boundary conditions.

Figure 2 shows simulated compressive true stress-true strain curves for single-crystal micro-pillars having five different primary slip-plane inclination angles (θ's).
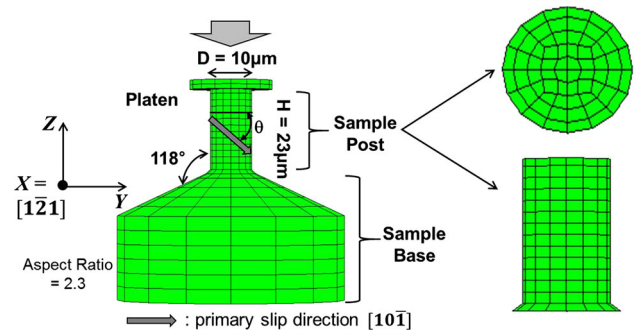

Fig. 1—The simulation geometry for the micro-pillar and the platen.

Table III. Input Constitutive Parameter Values for CP-FEM Simulations

C_{11}	247 GPa
C_{12}	147 GPa
C_{44}	125 GPa
$\dot{\gamma}_o$	0.001/s
m	0.03
$\hat{g}_o$	420 MPa
η	1/3
b	2.5×10^{-10} m
ρ_0	10^{11}/m²
k_1	6.1×10^7/m
k_2	7.84
$A^{\alpha\beta}$	A_{SH} (0.04), A_{CO} (0.07), A_{CS} (0.07), A_{HL} (0.07), A_{GL} (0.38), A_{LC} (0.76)

C_{11}, C_{12}, and C_{44} are elastic constants.

Table I. Twelve Octahedral Slip Systems Used for the Current Constitutive Model

1	$(111)[0\,1\,\bar{1}]$
2	$(111)[\bar{1}0\,1]$
3	$(111)[1\,\bar{1}0]$
4	$(\bar{1}\bar{1}1)[0\,1\,1]$
5	$(\bar{1}\bar{1}1)[101]$
6	$(\bar{1}\bar{1}1)[\bar{1}10]$
7	$(\bar{1}11)[01\bar{1}]$
8	$(\bar{1}11)[101]$
9	$(\bar{1}11)[\bar{1}10]$
10	$(1\bar{1}1)[0\bar{1}\bar{1}]$
11	$(1\bar{1}1)[\bar{1}01]$
12	$(1\bar{1}1)[110]$

Table II. Five Crystal Orientations Having $(111)[\bar{1}01]$ as a Primary Slip System and Showing Different Primary Slip-Plane Inclination Angles and Corresponding Primary SFs and ΔSFs (Schmid Factor Difference Between The Primary and Secondary Slip Systems)

θ (deg)	$(\varphi_1, \Phi, \varphi_2)$ (deg)	|SF|	ΔSF	Secondary Slip System
36.3	(60, 42, −8)	0.4481	0.043	$(111)[1\bar{1}0]$
39.5	(63, 40, −12)	0.4632	0.069	$(\bar{1}11)[101]$
42.8	(67, 39, −17)	0.4689	0.086	$(111)[1\bar{1}0]$
45.8	(71, 37, −21)	0.4741	0.099	$(\bar{1}11)[101]$
48.7	(74, 37, −26)	0.4666	0.113	$(111)[1\bar{1}0]$

Simulated flow curves show gradual softening after the onset of plasticity for $\theta = 42.8$, 45.8, and 48.7 deg. However, almost plateau-like (zero strain hardening) plastic flow curves followed by rapid softening after about 7 pct strain were observed for $\theta = 36.3$ and 39.5 deg. Further details about flow softening behaviors for different θ values will be discussed later.

Figure 3 shows the Y–Z front and sectional views of simulated total accumulated slip shear ($\sum \gamma^\alpha$) contours of micro-pillars at 10 pct strain for five different θ's. Here, note that the initial primary slip direction is from upper left to bottom right for all cases. In Figure 3, the simulated micro-pillar deformation for $\theta = 36.3$ and

Fig. 2—Simulated compressive true stress-true strain curves for $\theta = 36.3$, 39.5, 42.8, 45.8, and 48.7 deg. The inset in the figure illustrates an primary slip-plane inclination angle θ.

39.5 deg complies with the compressive deformation due to original primary slip $((111)[\bar{1}01])$ shear, and leaves inactive slip zones (so called "dead zone") in the bottom left and upper right regions of the micro-pillar. For $\theta = 42.8$, 45.8, and 48.7 deg, however, simulated plastic shear deforms the micro-pillar in a different direction, compared to the case for $\theta = 36.3$ and 39.5 deg, and leaves inactive slip zones in the upper left and bottom right regions. This difference is clearly seen in the look-down (X–Y) view of the top surface of the micro-pillar after 10 pct strain, as shown in Figure 4. To clarify the origin of this difference, the evolution of the maximum resolved shear stress ($\tau_{max}{}^\alpha$) distribution before and after the onset of plasticity was compared between the cases for $\theta = 36.3$ and 48.7 deg, and the resulting $\tau_{max}{}^\alpha$ contours are shown in Figure 5 as a function of strain. Here, note that the onset of plasticity took place at about 0.44 pct strain for both cases. In Figure 5, the $\tau_{max}{}^\alpha$ distribution shows essentially no difference between $\theta = 36.3$ and 48.7 deg in the elastic regime (0.38 pct strain in Figure 5). However, after the onset of plasticity the evolution of the $\tau_{max}{}^\alpha$ distribution took a clearly different path between the two cases. For the case of $\theta = 36.3$ deg, the $\tau_{max}{}^\alpha$ distribution gradually evolves such that primary slip is globally organized in a direction coincident with the primary slip direction ($[\bar{1}01]$). For the case of $\theta = 48.7$ deg, however, the evolution of the $\tau_{max}{}^\alpha$ distribution indicates that primary slip is globally organized in a direction from the upper right to bottom left of the micro-pillar. Such a difference in the evolution of the $\tau_{max}{}^\alpha$ distribution between $\theta = 36.3$ and 48.7 deg eventually leads to completely different micro-pillar deformations at 10 pct strain, as shown in Figure 3.

Results from Figures 3, 4 and 5 indicate that the compressive deformation behavior of the single-slip-oriented micro-pillar predicted by CP-FEM is highly sensitive to the primary slip-plane inclination angle θ, and such a sensitivity becomes effective only after the
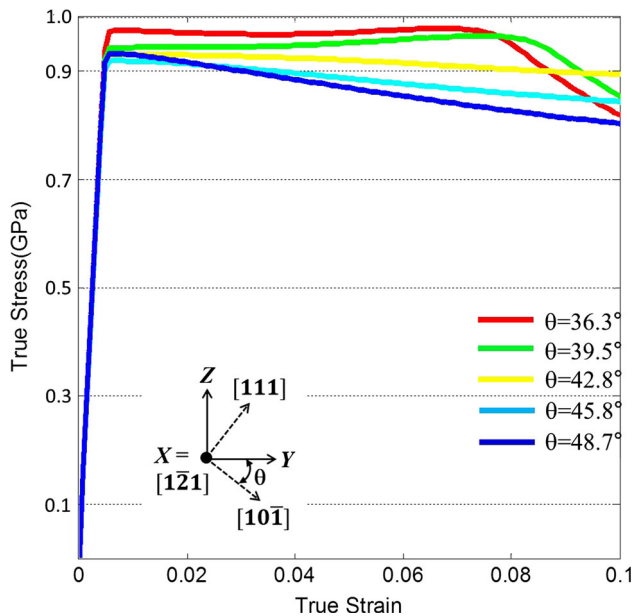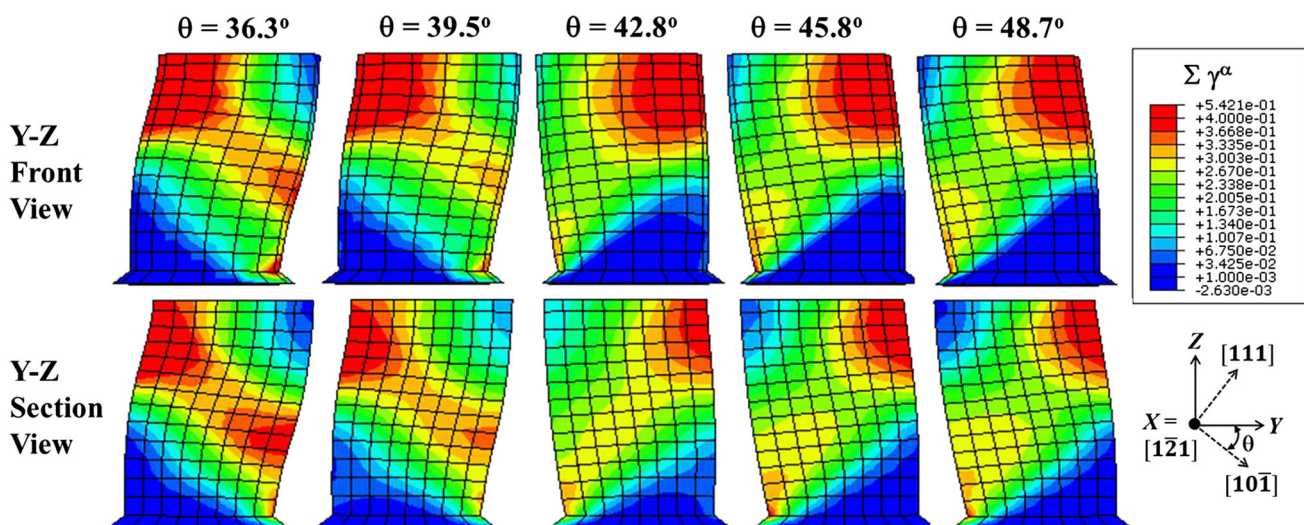

Fig. 3—Y–Z front and sectional views of simulated total accumulated slip shear contours at 10 pct strain for $\theta = 36.3$, 39.5, 42.8, 45.8, and 48.7 deg.

onset of plasticity. The θ sensitivity of the micro-pillar in CP-FEM is caused by the interaction between slip kinematics and the geometric constraint of the micro-pillar (within the continuum framework) under the applied compressive boundary conditions. Kuroda[25,26] showed that the plastic deformation mode predicted by the CP-FEM simulation was consistent with the result from a simple slip kinematics-driven calculation for $[\bar{1}23]$ compression, which is equivalent to $\theta = 49.1$ deg. From Figure 3, the critical θ value that switches the simulated global deformation mode seems to lie between 39.5 and 42.8 deg. Of course, this critical θ value will vary, depending on the micro-pillar geom-
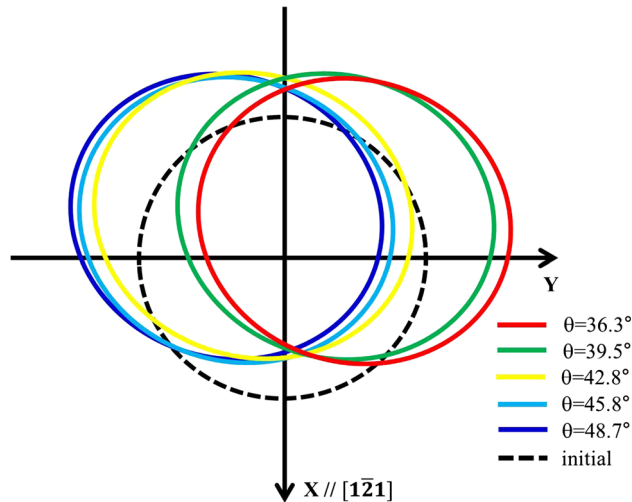
etry, applied boundary conditions, the choice of the constitutive model, *etc*. As slip system driven plastic shear takes different global paths, depending on the magnitude of θ, the global deformation of the micro-pillar seems to be facilitated by the intensive shear zone, which forms in the upper left toward the bottom right for the low θ and the upper right toward the bottom left for the high θ (Figure 3), and leads to different $X–Y$ in-plane displacements of top surfaces of micro-pillars as shown in Figure 4. Here, the shape change of top surfaces of micro-pillars shown in Figure 4 (ellipsoids elongated along the global Y axis) is mainly due to primary slip as the primary slip direction $[\bar{1}01]$ projected on the global $X–Y$ plane is parallel to the Y axis (see Figure 4).

Now, accumulated shear of selected major slip systems (original primary, secondary slip systems and slip system #4) for the cases of $\theta = 36.3$ and 48.7 deg were calculated from CP-FEM simulations and plotted in Figure 6 as a function of compressive axial strain. Here, in the case of $\theta = 36.3$ deg, one can clearly see the gradual dominance of slip #4, $(\bar{1}\bar{1}1)[0\bar{1}\bar{1}]$, after about 7 pct strain. This is consistent with the initiation of flow softening at about 7 pct strain for $\theta = 36.3$ deg, as shown in Figure 2. For the further investigation, the lattice rotation contour map and the primary slip system map at 10 pct strain were compared between $\theta = 36.3$ and 48.7 deg, as shown in Figure 7. Here, the primary slip system was determined by comparing the amount of incremental shear for each slip system. In Figure 7, one can see the development of a lattice rotation band across the micro-pillar and the resulting primary slip system changes from #2 $(111)[\bar{1}01]$ slip to #4 $(\bar{1}\bar{1}1)[0\bar{1}\bar{1}]$ slip for $\theta = 36.3$ deg. For $\theta = 48.7$ deg, however, the lattice rotation seems to be neither pronounced nor globally organized, compared to
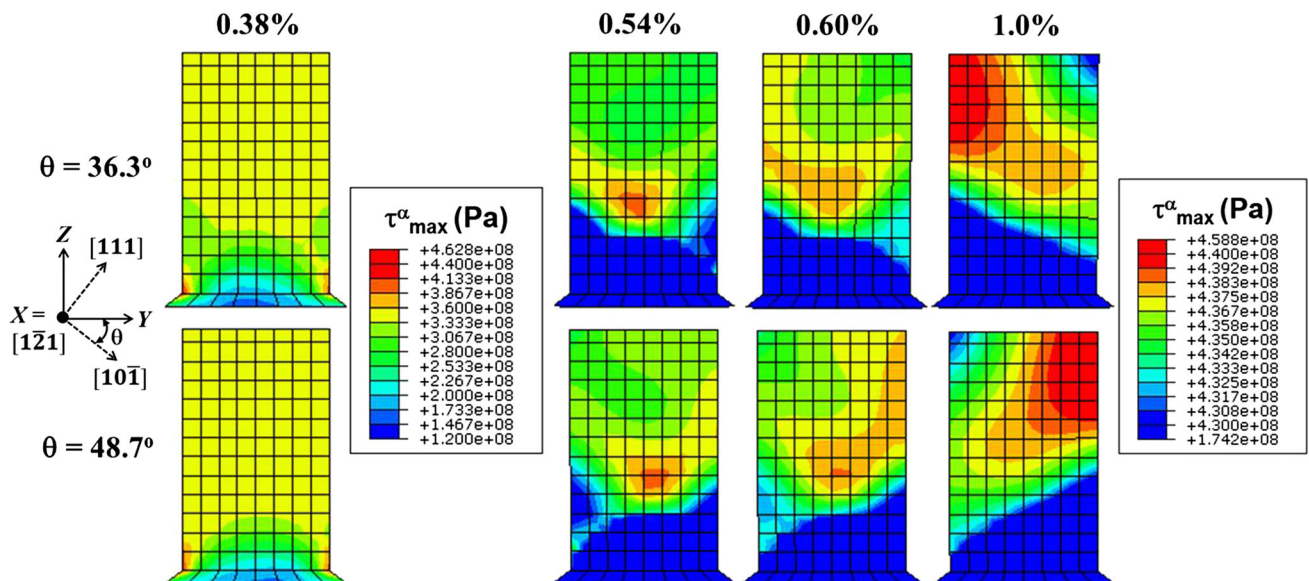

Fig. 4—Movement and shape change of top surfaces of micro-pillars with $\theta = 36.3$, 39.5, 42.8, 45.8, and 48.7 deg after 10 pct strain. Note that the primary slip (#2, $(111)[\bar{1}01]$) direction projected on the $X–Y$ plane is parallel to the Y direction.

Fig. 5—Y–Z sectional views of simulated maximum resolved shear stress contours for $\theta = 36.3$ and 48.7 deg at 0.38, 0.54, 0.60, and 1.0 pct strains. Note that the onset of plasticity takes place at about 0.44 pct strain.

θ = 36.3 deg, keeping slip #2 as a primary slip system even at 10 pct strain (Figure 7). Perhaps, this is due to the inconsistency between the primary slip direction (from the upper left to the bottom right) and the global plastic deformation (from the upper right to the bottom left, see Figures 3 and 5) for the high θ, which leaves plastically dead zones in the upper left and bottom right regions of the micro-pillar (Figure 3).

Combining the results from Figures 3, 5, 6 and 7, flow softening after the onset of plasticity for the case of high θ values (θ = 42.8, 45.8, and 48.7 deg) in Figure 2 seems to be associated with the globally organized deformation of the micro-pillar, which is facilitated by the clear distinction between the intensive shear zone

Fig. 6—Variation of accumulated shear of major slip systems for θ = 36.3 and 48.7 deg as a function of axial compressive strain.

(running from the upper right toward the bottom left) and the plastically "dead (inactive) zone" (in the upper left and bottom right) in Figure 3. Here, note that a different degree of flow softening (highest in θ = 48.7 deg, followed by θ = 45.8 and 42.8 deg) is consistent with the order in primary slip dominance, as confirmed by ΔSF differences in Table II. In the case of low θ values (θ = 36.3 and 39.5 deg), however, almost zero strain hardening up to about 7 pct strain was observed in Figure 2. This seems to be due to the 'weak' dominance of primary slip, compared to the case of high θ values, as indicated by relatively low ΔSF values (0.043 for θ = 36.3 and 0.069 for θ = 39.5 deg) in Table II. Also, flow softening after about 7 pct strain (in Figure 2) is believed to be associated with the transition of a primary slip system (from #2 to #4 as implied in Figures 6 and 7), which was facilitated by the organized intensive shear band (from the top left toward the bottom right) in Figure 3 and the consequent lattice rotation across the micro-pillar in Figure 7.

The θ sensitivity of the micro-pillar deformation shown in Figures 2, 3, 4, 5 and 7 was for the friction-free condition at the contact between the platen and the top surface of the micro-pillar. In order to assess the influence of the friction condition on the θ sensitivity, non-zero coefficients of friction (0.01 and 0.1) were applied to the contact between the platen and the micro-pillar, and the resulting accumulated slip shear contour plots (at 10 pct compressive strain) are shown in Figure 8. When a very small value of the coefficient of friction (0.01) was applied, the θ sensitivity still exists (even though the total accumulated slip shear contour shows a slight change in Figure 8, compared to the friction-free case). However, when the coefficient of friction was increased to 0.1, the θ sensitivity of the global shape change of the micro-pillar was significantly
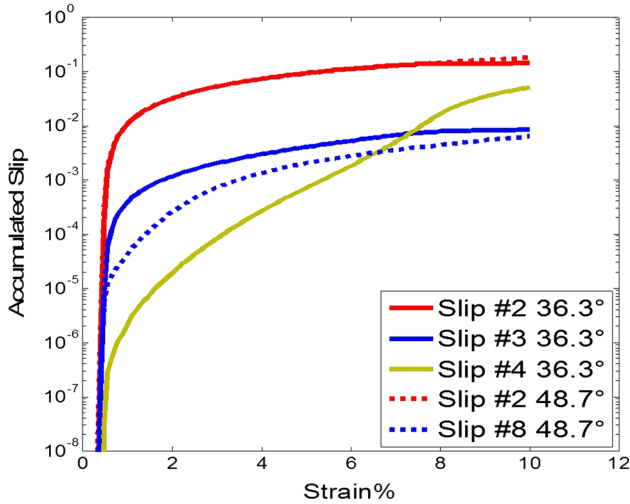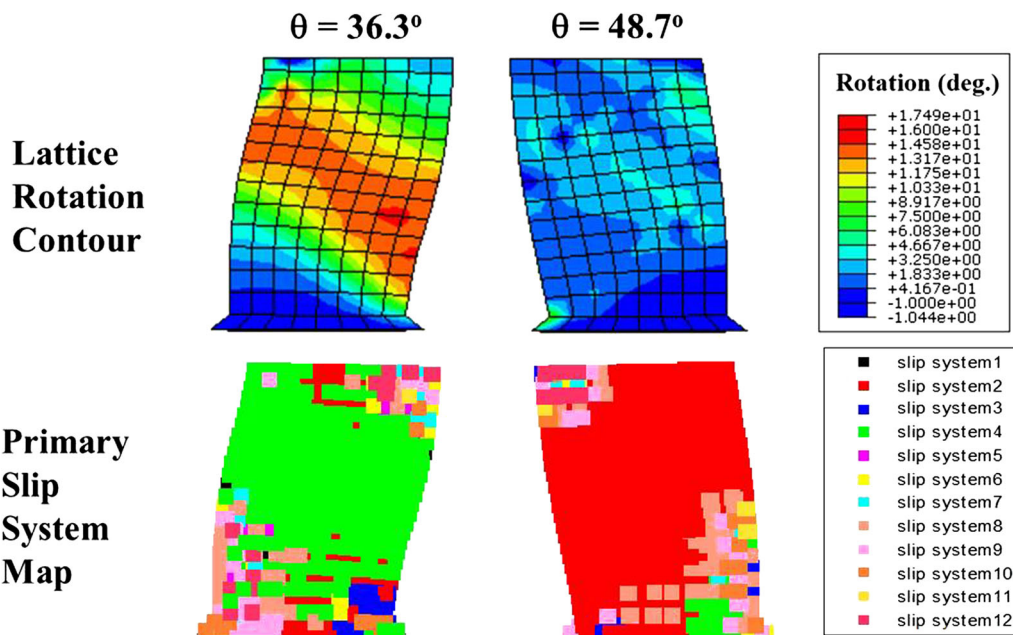

Fig. 7—Y–Z sectional views of the lattice rotation contour and the primary slip system map for θ = 36.3 and 48.7 deg at 10 pct strain.
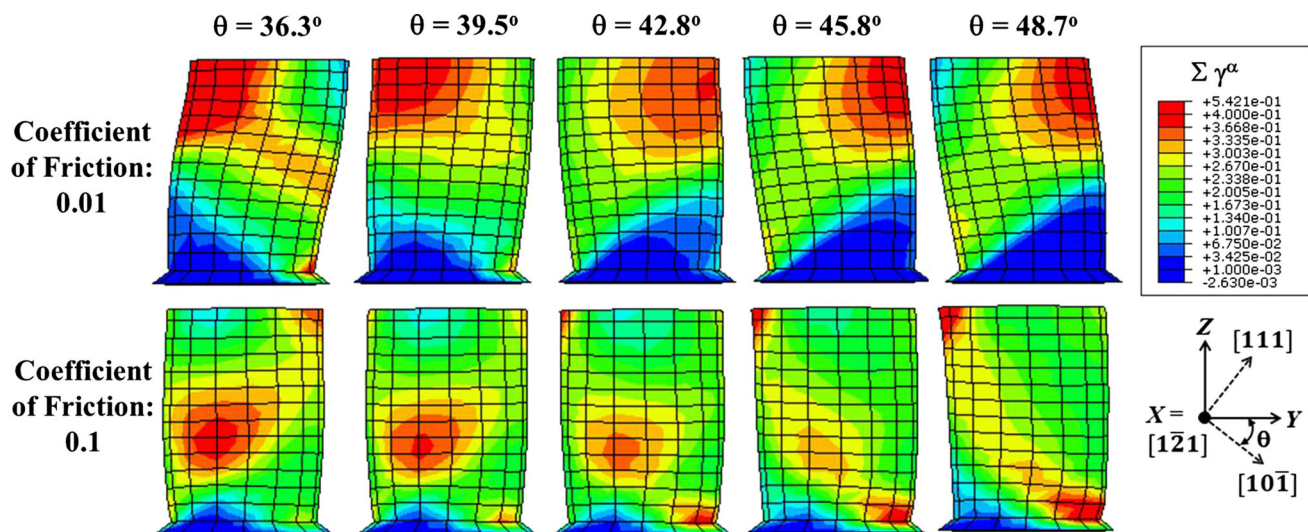
Fig. 8—Y–Z front views of simulated total accumulated slip shear contours for two different coefficients of friction (0.01 and 0.1) at 10 pct strain for θ = 36.3, 39.5, 42.8, 45.8, and 48.7 deg.

reduced. In this case, there seems to be no significant difference in the shape change of the micro-pillar as a function of θ even after 10 pct compression, even though total accumulated slip shear contours show a weak dependence of θ (see the bottom half of Figure 8). Here, note that by increasing the coefficient of friction to 0.1 the formation of the intensive shear zone was significantly reduced in the upper left or upper right regions of the micro-pillar, compared to the cases for the friction-free (Figure 3) and very small friction (the upper half of Figure 8). This is probably due to the increased lateral constraint (caused by the applied friction) on the top surface of the micro-pillar.[12,27] Such a lateral constraint suppresses slip activities near the top surface of the micro-pillar, and tends to prevent the formation of the near-surface intensive shear zone, consequently inhibiting the diagonally organized global shear deformation, which was observed in the friction-free and very small friction cases (Figures 3 and 8).

CP-FEM simulations were performed for the compressive deformation of single-slip-oriented single-crystal micro-pillars with different primary slip-plane inclination angles (θ's). The simulated global plastic deformation of the micro-pillar took two different paths, which are separated by the magnitude of the θ. For the low θ, the intensive plastic deformation zone was formed across the micro-pillar in a direction parallel to the original primary slip direction, and the resulting lattice rotation caused the transition of the primary slip system after about 7 pct strain, leading to softening of the flow curve. For the high θ, however, the plastic deformation of the micro-pillar was organized in a direction different from the low θ case, which led to the inactive lattice rotation throughout the micro-pillar due to the inconsistency between the primary slip direction and the global plastic deformation flow. The θ sensitivity of the simulated compressive deformation of the micro-pillar seemed to be associated with the continuum-based geometric constraint of the micro-pillar combined with implemented slip kinematics. That sensitivity suggests for example that small errors in crystal orientation lead to fundamentally different kinematics constraint for micro-pillar deformation. The validity of the θ sensitivity in microcompression experiments is believed to heavily depend upon mechanical and geometrical constraints of the micro-pillar in actual tests, as the θ sensitivity in CP-FEM simulations is expected to vary with the micro-pillar geometry, applied boundary conditions and the choice of the crystal plasticity constitutive model. In particular, the present CP-FEM simulations confirmed that the θ sensitivity shows a strong dependence of the friction condition at the contact between the platen and the micro-pillar.

REFERENCES

1. M.D. Uchic and D.M. Dimiduk: *Mater. Sci. Eng. A*, 2005, vols. 400–401, pp. 268–78.
2. H. Zhang, B.E. Schuster, Q. Wei, and K.T. Ramesh: *Scripta Mater.*, 2006, vol. 54, pp. 181–86.
3. C. Rehrl, S. Kleber, T. Antretter, and R. Pippan: *J. Phyics: Conf. Ser.*, 2010, vol. 240, p. 012157.
4. H. Zhang, B.E. Schuster, Q. Wei, and K.T. Ramesh: *Scripta Mater.*, 2006, vol. 54, pp. 181–86.
5. D.M. Dimiduk, M.D. Uchic, and T.A. Parthasarathy: *Acta Mater.*, 2005, vol. 53, pp. 4065–77.

6. Michael.D. Uchic and Dennis.M. Dimiduk: *Mater. Sci. Eng. A*, 2005, vols. 400–401, pp. 268–78.
7. Y. Yang, J.C. Ye, J. Lu, F.X. Liu, and P.K. Liaw: *Acta Mater.*, 2009, vol. 57, pp. 1613–23.
8. Z. Zhao, M. Ramesh, D. Raabe, A.M. Cuitino, and R. Radovitzky: *Int. J. Plast.*, 2008, vol. 24, pp. 2278–97.
9. P.A. Shade, M.D. Uchic, D.M. Dimiduk, G.B. Viswanathan, R. Wheeler, and H.L. Fraser: *Mater. Sci. Eng. A*, 2012, vol. 535, pp. 53–61.
10. Y.S. Choi, T.A. Parthasarathy, D.M. Dimiduk, and M.D. Uchic: *Mater. Sci. Eng. A*, 2005, vol. 397, pp. 69–83.
11. Y.S. Choi, M.D. Uchic, T.A. Parthasarathy, and D.M. Dimiduk: *Scripta Mater.*, 2007, vol. 57, pp. 849–52.
12. D. Raabe, D. Ma, and F. Roters: *Acta Mater.*, 2007, vol. 55, pp. 4567–83.
13. R. Maaß, S. Van Petegem, D. Ma, J. Zimmermann, D. Grolimund, F. Roters, H. Van Swygenhoven, and D. Raabe: *Acta Mater.*, 2009, vol. 57, pp. 5996–6005.
14. D. Peirce, R.J. Asaro, and A. Needleman: *Acta Mater.*, 1982, vol. 30, pp. 1087–1119.
15. E. Heripre, M. Dexet, J. Crepin, L. Gelebart, A. Roos, M. Bornert, and D. Caldemaison: *Int. J. Plast.*, 2007, vol. 23, pp. 1512–39.
16. D. Peirce, R.J. Asaro, and A. Needleman: *Acta Mater.*, 1983, vol. 31, pp. 1951–76.
17. Y. Zhou, K.W. Neale, and L.S. Toth: *Int. J. Plast.*, 1993, vol. 9, pp. 961–78.
18. J.P. Hirth and J. Lothe: *Theory of Dislocations*, MacGraw-Hill, New York, 1982.
19. P. Franciosi and A. Zaoui: *Acta Mater.*, 1982, vol. 30, pp. 2141–51.
20. P. Franciosi and A. Zaoui: *Acta Mater.*, 1982, vol. 30, pp. 1627–37.
21. H. Mecking and U.F. Kocks: *Acta Mater.*, 1981, vol. 29, p. 173.
22. P. Shanthraj and M.A. Zikry: *Acta Mater.*, 2011, vol. 59, pp. 7695–7702.
23. S.A. Tajalli, M.R. Movahhedy, and J. Akbari: *Comput. Mater.*, 2014, vol. 86, pp. 79–87.
24. Y. Huang: "A User-material Subroutine Incorporating Single Crystal Plasticity in the ABAQUS Finite Element Program", Harvard Univ., 1991.
25. M. Kuroda: *Acta Mater.*, 2013, vol. 61, pp. 2283–88.
26. M. Kuroda and V. Tvergaard: *Int. J. Solids Struct.*, 2009, vol. 46, pp. 4396–4408.
27. P.A. Shade, R. Wheeler, Y.S. Choi, M.D. Uchic, D.M. Dimiduk, and H.L. Fraser: *Acta Mater.*, 2009, vol. 57, pp. 4580–87.